Numerical Simulation of Hybrid Sliding-Rocking (HSR) Columns subjected to Earthquake Excitation

Mohammad Salehi[1], Petros Sideris[2] and Abbie B. Liel[3]

Abstract:
This paper introduces a novel element formulation for the dynamic analysis of bridges incorporating post-tensioned segmental columns with *hybrid sliding-rocking* (HSR) joints distributed over their height. These columns are termed "HSR columns". Bridges with HSR columns combine construction rapidity with superior seismic performance through joint sliding and rocking, thereby offering large deformation capacity with low damage, energy dissipation and self-centering properties. HSR columns are typically designed, under quasi-static (single-mode) conditions, to exhibit rocking at the end joints and sliding at the intermediate joints over the column height. However, when HSR columns are subjected to arbitrary dynamic loading, any joint can exhibit sliding or rocking or both, depending on the intensity and frequency content of the applied load. As a result, there is a need for models capable of predicting such complex responses. The proposed two-node HSR element formulation combines a *gradient inelastic (GI) flexibility-based (FB) beam-column element formulation* that accounts for member material deformations and joint rocking, with a *hysteretic friction model* that accounts for joint sliding. Joint rocking is considered within the GI FB element via a joint cross-section of zero tensile strength. The proposed HSR element addresses major deficiencies of existing modeling approaches, including strain localization and loss of objectivity (lack of convergence with mesh refinements) due to the cross-section of zero tensile strength. The proposed HSR element formulation is utilized to simulate two past experiments: a quasi-static test on an HSR column; and a shake table test on a single-span bridge with two single-column HSR piers. None of the computational simulations exhibited instabilities in the numerical solution, which are common in analyses with models including friction elements subjected to rapidly fluctuating contact loads, demonstrating the good stability properties of the proposed HSR element formulation. The analysis results matched the test data reasonably well, particularly in terms of peak forces and displacements, demonstrating that the proposed formulation can be used to further investigate the design and performance of HSR systems.

---

[1] Graduate Research Assistant – Ph.D. Student, Department of Civil, Environmental and Architectural Engineering, University of Colorado at Boulder, Boulder, CO, 80309, U.S.A. E-mail: Mohammad.SalehiNajafabadi@colorado.edu

[2] Assistant Professor, Department of Civil, Environmental and Architectural Engineering, University of Colorado at Boulder, Boulder, CO, 80309, U.S.A. E-mail: Petros.Sideris@colorado.edu

[3] Associate Professor, Department of Civil, Environmental and Architectural Engineering, University of Colorado at Boulder, Boulder, CO, 80309, U.S.A. E-mail: Abbie.Liel@colorado.edu

Introduction

Nationally, the Federal Highway Administration of the U.S. Department of Transportation has led a major effort towards the development of Accelerated Bridge Construction (ABC) strategies as a means of reducing construction times, improving product quality, and reducing traffic delays (Marsh et al. 2011). Early research on ABC focused on improving construction rapidity, producing promising ABC applications for low seismicity areas (Freyermuth 1999; Figg and Pate 2004). More recent research efforts have focused on combining construction rapidity with improved seismic performance, particularly through the development of ABC column designs, since columns are the critical bridge components under seismic loading. These studies have led to two types of column designs:

- Prefabricated monolithic columns (usually without post-tensioning) connected with the bent cap and the foundation through emulative (of monolithic) connections. Four types of these emulative connections may be found, namely, bar coupler connections (Tazarv and Saiidi 2013; Pantelides et al. 2014), grouted duct connections (Matsumoto et al. 2008; Haraldsson et al. 2009; Pang et al. 2010; Restrepo et al. 2011), gap pocket connections (Matsumoto et al. 2008; Restrepo et al. 2011; Weinert 2011), and member socket connections (Weinert 2011; Lehman and Roeder 2012; Haraldsson et al. 2013; White 2014).
- Prefabricated monolithic or segmental columns with end rocking joints and internal unbonded post-tensioning (Mander and Cheng 1997; Hewes and Priestley 2002; Restrepo et al. 2011; ElGawady and Dawood 2012). Unbonded post-tensioning provides large ductility capacity and self-centering capabilities. Supplemental energy dissipation to control displacement demands is provided either by internal partially debonded yielding rebar crossing the rocking joints (Marriott et al. 2009; Ou et al. 2010a; Ou et al. 2010b; Motaref et al. 2014) or by externally attached yielding links at the rocking joints (Marriott et al. 2009). Damage control in the vicinity of the rocking joints can be provided through steel jacketing (Hewes 2007; Abdelkarim and ElGawady 2014; Guerrini et al. 2014), fiber reinforced polymer (FRP) composite jacketing (ElGawady and Dawood 2012), steel armoring (White 2014), as well as using high performance materials, such as engineered cementitious composites and ultra-high-performance concrete (Billington and Yoon 2004; Ichikawa et al. 2016), and polymeric materials (Shrestha et al. 2015; Nikoukalam and Sideris 2016; 2017).

The concept of bridges with *Hybrid Sliding-Rocking (HSR)* columns was introduced by Sideris (2012) and Sideris et al. (2014b); (2014c); (2015) to achieve ABC in regions of moderate and high seismicity. The HSR columns are precast concrete segmental columns incorporating internal unbonded post-tensioning (Fig. 1), sliding joints distributed over the column height, and rocking joints at the column ends. Joint sliding is achieved by introducing a thin layer of silicone material at the interface of the sliding joints to achieve a targeted coefficient of friction. Duct adaptors, which are pieces of PVC tubing of diameter larger than the diameter of the ducts, control joint sliding together with the unbonded tendons (Fig. 1). The diameter and height of duct adaptors control the peak sliding amplitude by adjusting the rate of increase of the tendon bearing forces with joint sliding, and are selected such that tendon shearing at the joint interface is prevented (Sideris et al. 2014c).

Compared to monolithic and post-tensioned rocking columns, HSR columns offer large deformation capacity without damage, via small sliding of multiple joints over the column height. Joint sliding also offers energy dissipation capabilities to control seismic displacement demands, and helps controlling peak forces and accelerations by partly acting as a multi-level seismic isolation

81 system. These properties have been confirmed through shake table testing of a large-scale bridge
82 (Sideris et al. 2014b; 2015) and quasi-static testing of large-scale columns (Sideris et al. 2014c),
83 conducted at the University at Buffalo. These studies further demonstrated the potential of the
84 HSR columns to control high frequency excitations, provide non-damaging response against tor-
85 sional loads (sustained via torsional joint sliding) and the capability to accommodate multiple sup-
86 port excitations and permanent support offsets with limited or no damage (Sideris 2012). Further
87 (computational) study of these experimentally observed properties as well as investigation of new
88 properties has been hindered by the lack of robust high-fidelity low-computational-cost models
89 capable of capturing the fundamental components of the response of the HSR columns, including
90 (Fig. 2): (*i*) combined sliding and rocking at the (deformable) joint interfaces, which results in
91 large concrete compressive damage in regions of high flexural demands, and (*ii*) interactions be-
92 tween the concrete segments and the unbonded post-tensioning tendons inside the ducts, which
93 control the sliding response of the joints via the bearing contact forces that apply to the concrete
94 segments in the vicinity of the sliding interface (at the connection of ducts and duct adaptors).
95   HSR columns are designed, under quasi-static first-mode conditions (i.e. by applying a lateral
96 load profile that is proportional to the fundamental mode shape, and neglecting inertia/damping
97 effects), to exhibit rocking at the end joints, where high flexural demands are expected, and sliding
98 at the intermediate joints over the column height. For these conditions, selection criteria for major
99 design variables, such as joint coefficient of friction, duct adaptor diameter and height, and dimen-
100 sions of the end segments, have been proposed by Sideris et al. (2014c), while a capacity spectrum
101 design methodology has been investigated by Madhusudhanan and Sideris (2015). However, under
102 arbitrary dynamic loading (e.g., earthquakes), any joint can exhibit sliding or rocking (or both),
103 depending on the intensity and frequency content of the applied load. Recent experimental studies
104 on a large-scale HSR bridge and large-scale HSR columns (Sideris 2012; Sideris et al. 2014b; c;
105 2015) have demonstrated this response complexity in the presence of dynamic loading (as opposed
106 to quasi-static loading), thereby emphasizing the need for robust numerical modeling techniques
107 capable of predicting the dynamic response of HSR columns.

Literature Review

Background in Structural Modeling of RC Rocking Members

110   Modeling of rocking members using three-dimensional (3D) finite element analysis, despite
111 providing reasonably accurate response predictions, requires extensive computational effort and
112 resources and has solely been considered for the analysis of individual rocking columns subjected
113 to monotonic quasi-static loading (Dawood et al. 2011; ElGawady and Dawood 2012; Dawood
114 and ElGawady 2013; Abdelkarim and ElGawady 2014).
115   For the dynamic analysis of rocking RC members, the most common approach to simulate
116 rocking joints has been through a set of compression-only two-node contact elements (Winkler's
117 spring approach), often of zero length, which are distributed over the joint interface and are rigidly
118 connected to the beam centerline (Spieth et al. 2004; Palermo et al. 2005; Marriott et al. 2009;
119 Sideris et al. 2010; Wang et al. 2011). If the response of these compression-only contact elements
120 is assumed to be linear elastic, the lateral strength of the column is overestimated, because essen-
121 tially the joint response is closer to that of a rigid interface, rather than a deformable interface.
122 Considering inelastic response for the compression-only contact elements improves predictions,
123 but this modeling approach still suffers from major issues, such as:

124 • It requires definition of an *equivalent element length* – even in the case of zero-length elements
125   – which significantly affects the predicted response (e.g., Marriott et al. 2009) and is difficult

126   to estimate and physically interpret. Estimation of this equivalent length requires component
127   testing data, rather than data from material testing.

128 • It assumes *constant strain distribution* over the length of the compression-only contact ele-
129   ments, despite the fact that several studies (e.g., Roh 2007; Roh and Reinhorn 2010) have
130   shown that the distribution of strain over the member length is nonlinear.

131 • It considers *no interactions between adjacent springs*, which is physically irrational, because
132   adjacent material volumes interact through shear stresses. As a result, they provide no support
133   against shear deformations, which should be accounted for through additional springs.

134 • It requires a *large number of compression-only contact elements* to capture the contact force
135   distribution with sufficient spatial resolution, resulting in a computationally-expensive solution
136   at the structure level, and increasing the probability of user error in the topological definition
137   of the contact elements and selection of their mechanical properties.

138   To avoid the weaknesses and physical irrationalities of the Winkler's spring approach, more
139 recent studies on RC rocking members have employed flexibility-/force-based (FB) beam-column
140 elements, also known as fiber FB elements, where the rocking member is usually modeled by a
141 single FB element and the rocking joint is modeled as a single cross-section with compression-
142 only material response (Kurama et al. 1999; Shen et al. 2006; Lee et al. 2007; Perez et al. 2007;
143 Ameli and Pantelides ; Bu et al. 2016). In that sense, joint rocking is incorporated within the frame-
144 work of the continuous classical beam theory and the compressive normal strain distribution over
145 the cross-section is inherently assumed to be linear during rocking. This approach has provided
146 more robust predictions of the response of rocking columns at a much lower computational cost.
147 However, because the compression-only cross-section is essentially a weak section that softens/de-
148 teriorates more quickly than its adjacent cross-sections that have tensile strength, the correspond-
149 ing FB element suffers from *strain localization* and *loss of objectivity* (Coleman and Spacone
150 2001; Sideris and Salehi 2016; Salehi and Sideris 2017). The phenomenon of *strain localization*
151 implies that the damage induced at the rocking section during softening cannot spread to adjacent
152 sections in the model. This is contrary to several experimental and numerical studies that have
153 shown that damage induced at the rocking interface spreads over the column length (Roh 2007;
154 Ou et al. 2010b; Roh and Reinhorn 2010; Sideris 2012). The *loss of objectivity* represents the
155 observed divergence, as opposed to convergence, of the predicted response with mesh refinements
156 (i.e., with increasing the number of integration points (IPs) over the length of FB elements). As a
157 result, for a low number of IPs, a slow deterioration would be predicted, whereas a large number
158 of IPs would result in rapid post-peak deterioration, neither of which would be correct. This sig-
159 nificant mesh sensitivity makes use of this approach unreliable.

160   ***Extension of Rocking Modeling to HSR Columns and Challenges***

161   The 3D finite element modeling approaches considered for rocking columns can also be ex-
162 tended to HSR columns by introducing friction at the contact between adjacent segments. Specif-
163 ically, Sideris (2015) built a comprehensive 3D finite element model of an HSR column
164 (ABAQUS, DS 2010), which was validated against data from a quasi-static test on an HSR column
165 (Sideris et al. 2014c) and used in a parametric monotonic pushover study that examined the effects
166 of design and loading parameters on the system response. In accordance with the observations
167 from analyses of rocking columns, that model, despite providing reasonably accurate predictions
168 of the experimental response, required long analysis times and extensive computational resources,
169 rendering dynamic analyses impractical.

170   Extension of the Winkler's spring approach to model the response of HSR columns requires
171 the use of compression-only two-node contact elements with lateral sliding (i.e., contact sliders).

172   In addition to the weaknesses indicated in the previous section, use of contact sliders in situations
173   where there are large rapid variations of the contact force during the analysis, as is the case for
174   sliding-rocking joints, results in high frequency fluctuations – also known as *chattering* – in the
175   numerical solution and instabilities and eventual convergence failure of the solution algorithm.
176   Adopting this approach, Sideris (2012) investigated the response of HSR columns using the struc-
177   tural analysis software SAP2000 (CSI 2009). The interaction between unbonded tendons and the
178   concrete segments was modeled using two-node gap elements. The corresponding models suffered
179   from major chattering and rapid convergence failure of the numerical solution algorithm shortly
180   after the onset of the first joint sliding, rendering this approach impractical for the dynamic analysis
181   of HSR columns.

182   The use of fiber FB elements to study RC rocking columns can be extended to study the re-
183   sponse of HSR columns by: (*i*) modeling each segment with at least one fiber FB element and
184   introducing a single friction spring at each sliding-rocking joint, in series with the fiber FB ele-
185   ments, and (*ii*) modeling the interaction between unbonded tendons and the concrete segments
186   using gap elements. Due to the presence of FB elements, this approach suffers from strain locali-
187   zation and loss of response objectivity, while, the friction spring cannot account for the variations
188   of pressure distribution over the joint interface. Spatial and temporal pressure variations are par-
189   ticularly important for cases with pressure-dependent coefficients of friction, as is the case for the
190   HSR columns. Specifically, both experimental and numerical studies (Sideris 2012; Sideris et al.
191   2014c; Sideris 2015) have shown that the sequence of initiation of joint sliding – from bottom to
192   top – in HSR columns results from the pressure-dependence of the coefficient of friction (quanti-
193   fied by Sideris (2012)) at the joint interface.

194   A recent attempt to integrate sliding and rocking within a continuum beam framework account-
195   ing for the spatio-temporal pressure variations at the joint cross-section was made by Salehi and
196   Sideris (2016). Salehi and Sideris (2016) introduced a two-node FB element capable of capturing
197   the rocking-sliding interactions at HSR joints by combining a FB beam-column element formula-
198   tion with an empirical law for the rocking rotation and a hysteretic friction model for the joint
199   sliding. The rocking empirical law considered a variable equivalent plastic hinge length based on
200   the contact depth during rocking. Although the computational predictions were in good agreement
201   with the test data, the empirical rocking law resulted in major instabilities of the numerical solution
202   algorithm. Response inconsistencies were observed under cyclic loading, because partial loss of
203   contact could occur at both sides of the cross-section, which was beyond the definition of the
204   "contact depth" considered in the empirical law, which only accounted for loss of contact at one
205   side due to monotonic loading conditions. Moreover, strain localization at the HSR joint was not
206   alleviated, causing convergence failures in the element-level iterative solution algorithm. Despite
207   its weaknesses, this formulation was the first to provide predictions of the dynamic response of
208   HSR columns with reasonable computational efficiency.

Scope

210   Building on the work of Salehi and Sideris (2016), this study introduces a novel FB beam-column
211   element formulation to simulate the response of HSR joints, thereby allowing the study of bridges
212   incorporating HSR columns under dynamic loading. The proposed formulation combines the fol-
213   lowing two components:

214   1. A gradient inelastic (GI) beam theory (Sideris and Salehi 2016; Salehi and Sideris 2017), which
215   eliminates strain localization phenomena and is capable of simulating member material defor-
216   mations and capturing joint rocking through compression-only section constitutive relations at

217   the location of the HSR segmental joint. Integrating fundamental concepts from gradient dam-
218   age and plasticity theories, the GI beam theory and the corresponding GI FB element formula-
219   tion eliminate strain localization phenomena by associating the *macroscopic* section strains of
220   the strain vs. displacement equations with the *material/local* section strains of the constitutive
221   relations, via a set of *gradient nonlocality relations*. The gradient nonlocality relations intro-
222   duce a *characteristic length* that represents the spreading of locally-induced damage over its
223   vicinity. As a result, locally-induced compressive damage due to joint rocking is spread away
224   from the rocking joint, as dictated by the characteristic length, providing objective response
225   (i.e. convergent with progressive mesh refinements). The characteristic length may be regarded
226   as an equivalent plastic hinge length. Fundamentally, it is the nonlocality relations that make
227   the GI beam theory free of strain singularities and the GI FB element formulation objective
228   (Sideris and Salehi 2016).
229 2. A pressure-dependent friction model in the form of a uniaxial plasticity formulation to simulate
230   joint sliding at the location of HSR segmental joints. The effect of the temporal variability of
231   the pressure is considered via a pressure-dependent coefficient of friction on the basis of the
232   test data by Sideris (2012). The spatial variability of the pressure is accounted for through the
233   consideration of the friction model over various locations (cross-section fibers) at the joint
234   interface, as opposed to the use of a single friction spring at each sliding joint.

235   The resulting HSR element formulation is implemented by the authors in the open-source struc-
236   tural analysis program OpenSees (McKenna et al. 2000) and used to simulate the response of HSR
237   columns from two past experimental studies: (*i*) a quasi-static test on an HSR column, and (*ii*) a
238   shake table test on a single-span bridge with two single-column HSR piers. The interaction of the
239   unbonded tendons with the concrete segments is modeled using gap elements. The predicted re-
240   sponses are compared with the test data to validate the efficacy of the proposed modeling approach
241   and identify modeling needs to be addressed in future studies.

Proposed HSR Element Formulation

243   The proposed HSR element is essentially a *two-node GI beam with a sliding-rocking joint* along
244   its length or at any of its two ends. The formulation of the HSR element combines a *GI FB formu-
245   lation* that accounts for material deformations and joint rocking, with a *hysteretic friction model*
246   that accounts for joint sliding. Rocking is considered within the GI FB formulation through section
247   constitutive relations with zero tensile strength at the HSR joint. The total member end displace-
248   ments (Fig. 3 (c)) are obtained through summation of member end displacements of the GI formu-
249   lation accounting for material deformations and joint rocking (Fig. 3 (a)) and member end dis-
250   placements caused by joint sliding (Fig. 3 (b)) via the hysteretic friction model.

251   Apart from eliminating strain localization phenomena and providing response objectivity, use
252   of the GI FB element formulation also offers improved stability and convergence properties of the
253   numerical solution (Sideris and Salehi 2016), and predictions of the section strain field in the vi-
254   cinity of HSR joint (damage propagation), which has not been possible with the other FB formu-
255   lations (Salehi et al. 2017).

System of Equations

Gradient Inelastic Flexibility-Based Element Formulation

258   Compared to the classical (local) beam theory, founded on Navier's assumption of plane sections,
259   the GI beam theory (Sideris and Salehi 2016; Salehi and Sideris 2017) introduces a set of gradient
260   nonlocality relations to associate macroscopic section strains (in the strain-displacement equa-

5

261 tions) with *material/local* section strains (in the constitutive relations). As a result, unlike the clas-
262 sical beam theory that is described by three sets of equations, the GI theory comprises four sets of
263 equations: (*i*) macroscopic section strain-displacement equations, (*ii*) force equilibrium equations,
264 (*iii*) section constitutive relations, and (*iv*) nonlocality relations.
265   The *macroscopic section strain-displacement equations* follow the Navier's assumption of
266 "plane sections" and are expressed as:

$$\begin{cases} \varepsilon_o(x) = u_{o,x}(x) \\ \phi(x) = \theta_{,x}(x) \\ \gamma_{xy}(x) = v_{o,x}(x) - \theta(x) \end{cases} \tag{1}$$

267 where $\varepsilon_0(x)$, $\phi(x)$, and $\gamma_{xy}(x)$ are the macroscopic axial strain, the macroscopic curvature, and
268 the macroscopic shear strain at the coordinate x on the reference axis, respectively (Fig. 4), while
269 $u_o(x)$, $v_o(x)$, and $\theta(x)$ are the axial displacement, the transverse displacement, and the rotation
270 of the beam with respect to the reference axes at the location x, respectively (Fig. 4). The notation
271 subscript ",x" stands for the first derivative with respect to x. These displacements do not include
272 contributions from joint sliding, because joint sliding is solely considered in the friction model, as
273 described later.
274   The *force equilibrium equations* for the undeformed beam under quasi-static loading conditions
275 and without body loads are:

$$\begin{cases} N_{,x}(x) = 0 \\ V_{,x}(x) = 0 \\ M_{,x}(x) + V(x) = 0 \end{cases} \tag{2}$$

276 where $N(x)$, $V(x)$, and $M(x)$ are the axial force, the shear force, and the moment on the section
277 located at x.
278   The *section constitutive relations* determine the section forces based on the *material/local* sec-
279 tion strains and the loading history. These relations are stated as:

$$\vec{D}(x) = \vec{f}_{ms}\left(\vec{d}^e(x)\right) \quad \text{with} \quad \begin{cases} \vec{D}(x) = \begin{bmatrix} N(x) & M(x) & V(x) \end{bmatrix}^T \\ \vec{d}^e(x) = \begin{bmatrix} e_o(x) & \kappa(x) & s_{xy}(x) \end{bmatrix}^T \end{cases} \tag{3}$$

280 where $\vec{f}_{ms}(\cdot)$ represents the constitutive relations in vector form, which are determined based on
281 the respective cross-section geometric and mechanical properties. Also, $\vec{D}(x)$ is the vector of sec-
282 tion forces at the coordinate x, and $\vec{d}^e(x)$ is the vector of *material/local* section strains, $e_0(x)$,
283 $\kappa(x)$, and $s_{xy}(x)$, representing *material/local* axial strain, curvature, and shear strain, respec-
284 tively, at the coordinate x. Equation (3) includes computation of normal and shear stresses over
285 the cross-section as function of the cross-section material/local strains and integration of these
286 stresses to compute the moment, axial and shear force at the cross-section.
287   The *nonlocality relations*, which associate the *material/local* section strains (from the constitu-
288 tive relations, Eq. (3)) with their *macroscopic* counterparts (in the section strain-displacement
289 equations, Eq. (1)), are expressed as:

6

$$\vec{d}(x) - \frac{1}{2}l_c^2\vec{d}_{,xx}(x) = \vec{d}^e(x) \quad \text{with} \quad \vec{d}(x) = \begin{bmatrix} \varepsilon_o(x) & \phi(x) & \gamma_{xy}(x) \end{bmatrix}^T \tag{4}$$

290 where $\vec{d}(x)$ is the vector of *macroscopic* section strains, and l_c is the characteristic length, which
291 controls the extent of plasticity spreading in the neighborhood of the section experiencing soften-
292 ing – i.e. the HSR joint section, which is always the weakest cross-section of the element. The
293 notation subscript ",$_{xx}$" represents the second derivative with respect to x. The two boundary con-
294 ditions (BCs) needed to solve Eq. (4) are selected to be of Dirichlet type, imposing:

$$\vec{d}(0) = \vec{d}^e(0) \text{ and } \vec{d}(L) = \vec{d}^e(L) \tag{5}$$

295 where $x = 0$ and L are the coordinates of the element ends ($0 \le x \le L$). Although Eqs. (4) and (5)
296 ensure continuous macroscopic strain distributions, additional BCs are needed to bound the mate-
297 rial/local section strains and provide objective force vs. displacement response during strain local-
298 ization (Sideris and Salehi 2016; Salehi and Sideris 2017). Because the only section along the HSR
299 element (other than the end sections) which may experience strain localization is the HSR joint
300 section, an additional Dirichlet BC is permanently enforced at the HSR joint location, x_j, as:

$$\vec{d}(x_j) = \vec{d}^e(x_j) \tag{6}$$

301 **Hysteretic Friction Model**
302 The friction model is essentially a uniaxial plasticity model with a constant loading/unloading
303 stiffness, k_{fr}, and a yield/bounding surface defined as the product of the coefficient of friction, μ,
304 and the normal contact stress, $\sigma(x_j, y)$, which is negative in compression. The model can be
305 mathematically expressed as:

$$\dot{\tau}_{fr}(x_j, y) = k_{fr}\dot{u}_{sl} \quad \text{with} \quad |\tau_{fr}(x_j, y)| < \mu|\sigma(x_j, y)| \tag{7}$$

306 where $\dot{\tau}_{fr}(x_j, y)$ is the rate of the friction stress at the coordinate y over the joint cross section, and
307 $\dot{u}_{sl}$ is the rate of joint sliding. The contact stress is always non-positive, $\sigma(x_j, y) \le 0$. Also, the
308 coefficient of friction is taken to be pressure-dependent, with $\mu = f_\mu(\sigma(x_j, y))$, in accordance with
309 the experimental findings by Sideris (2012), as discussed later. The total friction force, V_{fr}, at the
310 joint is computed by integrating τ_{fr} over the joint cross-section area; thus, the *frictional constitutive*
311 *relation* at the HSR joint can be expressed in the following condensed algebraic form:

$$V_{fr} = f_{fr}(u_{sl}, k_{fr}, \mu\sigma(x_j, y)) \tag{8}$$

312 In addition, *shear force equilibrium* in the HSR joint yields:

$$V_{fr} = V(x_j) \tag{9}$$

313 *Analytical Solution*
314 The solution to the proposed HSR element formulation should consider together its two compo-
315 nents: (*i*) GI beam theory (Eqs. (1) through (4)), and (*ii*) hysteretic friction model (Eqs. (8) and
316 (9)).
317 Solution to the equations of the GI beam theory requires six boundary conditions (BCs),
318 namely, three end displacements and three end forces. Herein, these BCs are chosen in accordance
319 with the cantilever reference system shown in Fig. 5. Solving the force equilibrium equations of

320   Eq. (2), analytically, for the section forces, $\vec{D}(x)$, yields:

$$\vec{D}(x) = [b(x)]\vec{Q} \quad \text{with} \quad \begin{cases} \vec{Q} = [Q_1 \quad Q_2 \quad Q_3]^T \\ [b(x)] = \begin{bmatrix} 1 & 0 & 0 \\ 0 & 1 & L-x \\ 0 & 0 & 1 \end{bmatrix} \end{cases} \tag{10}$$

321   where $[b(x)]$ is the matrix of the section force shape functions, $\vec{Q}$ is the vector of end force BCs
322   (Fig. 5), and L is the element length.
323   Solution of the shear force equilibrium at the HSR joint (Eq. (9)) yields:

$$V_{fr} = [b_{fr}]\vec{Q} \quad \text{with} \quad [b_{fr}] = [0 \quad 0 \quad 1] \tag{11}$$

324   where $[b_{fr}]$ is the matrix of the friction force shape functions.

325   The total end displacements, $\vec{q}$ (Fig. 5), of the HSR element are determined as (Fig. 3):

$$\vec{q} = \vec{q}_{GI} + \vec{q}_{sl} \tag{12}$$

326   where $\vec{q}_{GI}$ is the vector of the end displacements obtained from the GI beam theory and attributed
327   to material deformations and joint rocking (Fig. 3 (a)), while $\vec{q}_{sl}$ is the vector of the end displace-
328   ments resulting from the joint sliding (Fig. 3 (b)). By the direct integration of the macroscopic
329   section strain-displacement equations (Eqs. (1)), $\vec{q}_{GI}$ is given by:

$$\vec{q}_{GI} = \int_0^L [b(x)]^T \vec{d}(x)dx \quad \text{with} \quad \vec{q}_{GI} = [q_{GI,1} \quad q_{GI,2} \quad q_{GI,3}]^T \tag{13}$$

330   The end displacements due to joint sliding, $\vec{q}_{sl}$, are determined as (Fig. 3(b)):

$$\vec{q}_{sl} = [b_{fr}]^T u_{sl} \quad \text{with} \quad \vec{q}_{sl} = [q_{sl,1} \quad q_{sl,2} \quad q_{sl,3}]^T \tag{14}$$

331   By assuming that the solution of the nonlocality relation (Eq. (4)) along with its BCs (Eqs. (5)
332   and (6)) has the form:

$$\vec{d}(x) = \vec{f}_{nl}(\vec{d}^e(x)) \tag{15}$$

333   and substituting Eq. (3) into Eq. (10), Eq. (8) into Eq. (11), and Eqs. (13) and (14) into Eq. (12),
334   the final system of equations is obtained as:

$$\begin{cases} [b(x)]\vec{Q} - \vec{f}_{ms}(\vec{d}^e(x)) = \vec{0} \\ [b_{fr}]\vec{Q} - f_{fr}(u_{sl}, k_{fr}, \mu\sigma(x_j, y)) = \vec{0} \\ \vec{q} - \int_0^L [b(x)]^T \vec{f}_{nl}(\vec{d}^e(x))dx - [b_{fr}]^T u_{sl} = \vec{0} \end{cases} \tag{16}$$

335   The first of Eqs. (16) represents the GI beam equilibrium and constitutive relations; the second of
336   Eqs. (16) represents the shear force equilibrium and hysteretic friction model at the HSR joint; and
337   the third of Eqs. (16) represents the displacement compatibility accounting for contributions from
338   material deformations, joint rocking, and joint sliding. For any given end displacements, $\vec{q}$, Eqs.

339 (16) constitute a system of three equations in three unknowns, namely, $\vec{Q}$, $\vec{d}^e(x)$, and u_{sl}.

340 The element tangent flexibility matrix, $[f_{el}]$, is determined by using the chain rule and Eqs.

341 (16), as:

$$[f_{el}] = \frac{\partial \vec{q}}{\partial \vec{Q}} = \int_0^L [b(x)]^T [k_{nl}(x)][k_{ms}(x)]^{-1}[b(x)]dx + [b_{fr}]^T K_{fr}^{-1}[b_{fr}] \tag{17}$$

342 with:

$$\begin{cases} [k_{ms}(x)] = \left[\dfrac{\partial \vec{f}_{ms}}{\partial \vec{d}^e}(x)\right] \\[2ex] [k_{nl}(x)] = \left[\dfrac{\partial \vec{f}_{nl}}{\partial \vec{d}^e}(x)\right] \\[2ex] K_{fr} = \dfrac{\partial f_{fr}}{\partial u_{sl}} \end{cases} \tag{18}$$

343 where $[k_{ms}(x)]$ is the section tangent stiffness matrix, $[k_{nl}(x)]$ is the derivative of $\vec{d}(x)$ with

344 respect to $\vec{d}^e(x)$, and K_{fr} is the tangent frictional stiffness.

Discretization and Numerical Solution

346 Because the section constitutive relations ($\vec{f}_{ms}(\cdot)$ from Eq. (3)) and frictional constitutive rela-

347 tions ($f_{fr}(\cdot)$ from Eq. (8)) are nonlinear, and the nonlocality relations (Eq. (4)) do not accept closed

348 form solution for arbitrary material/local strain distributions, Eqs. (16) need to be solved numeri-

349 cally. For this purpose, the element is discretized into N integration points along its length, which

350 represent monitored cross-sections. The first of Eqs. (16) should be satisfied at all discrete IPs,

351 while the second of Eqs. (16) should be satisfied at the location, x_j, of the HSR joint. Also, the

352 integral in the third of Eqs. (16) is substituted by a weighted summation of the integrand values at

353 the IP locations. The resulting discretized form of Eqs. (16) is expressed as:

$$\begin{cases} [b(x_1)]\vec{Q} - \vec{f}_{ms}(\vec{d}^e(x_1)) = \vec{0} \\ [b(x_2)]\vec{Q} - \vec{f}_{ms}(\vec{d}^e(x_2)) = \vec{0} \\ \vdots \qquad\qquad \vdots \qquad\qquad \vdots \\ [b(x_N)]\vec{Q} - \vec{f}_{ms}(\vec{d}^e(x_N)) = \vec{0} \\ [b_{fr}]\vec{Q} - f_{fr}(u_{sl}, k_{fr}, \mu\sigma(x_j, y)) = \vec{0} \\ \vec{q} - \displaystyle\sum_{i=1}^N w_i [b(x_i)]^T \vec{f}_{nl}(\vec{d}^e(x_i)) - [b_{fr}]^T u_{sl} = \vec{0} \end{cases} \tag{19}$$

354 where x_i and w_i are the x-coordinate and the integration weight of the i-th IP ($i = 1, 2, \ldots, N$),

355 respectively, computed in accordance with a selected numerical integration method, with

356 $\sum_{i=1}^N w_i = L$. The joint location, x_j, should always match one of the selected IP locations. Also, the

357 first and last IPs should always be located at the element ends, as $x_1 = 0$ and $x_N = L$.

358 Equation (19) still requires the solution, $\vec{f}_{nl}\left(\vec{d}^e(x_i)\right)$, of the nonlocality relations (Eq. (4)), which

359 can be obtained in a discretized form, by enforcing them at each IP location, and replacing the

360 derivative with a 2nd order accurate central difference approximation. The resulting discretized

361 form of the nonlocality relations of Eq. (4) at the i-th IP location is:

$$\vec{d}(x_i) - \frac{1}{2}l_c^2\left(\frac{\vec{d}(x_{i+1}) - 2\vec{d}(x_i) + \vec{d}(x_{i-1})}{(\Delta x)^2}\right) = \vec{d}^e(x_i) \qquad (20)$$

362 where Δx is the distance between any two adjacent IPs, which are considered to be equally-spaced.

363 Combining Eq. (20) with the end BCs of Eqs. (5) and the additional BC of Eq. (6) for the location

364 of the HSR joint, yields:

$$\vec{d}_{tot} = [H]^{-1}\vec{d}_{tot}^e \quad \text{with} \quad \begin{cases} \vec{d}_{tot} = \left[\vec{d}^T(x_1) \quad \vec{d}^T(x_2) \quad \cdots \quad \vec{d}^T(x_N)\right]^T \\ \vec{d}_{tot}^e = \left[\vec{d}^{eT}(x_1) \quad \vec{d}^{eT}(x_2) \quad \cdots \quad \vec{d}^{eT}(x_N)\right]^T \end{cases} \qquad (21)$$

365 where $\vec{d}_{tot}^e$ and $\vec{d}_{tot}$ are vectors including the material/local and macroscopic section strains, re-

366 spectively, at all IP locations, while $[H]$ is a 3N-by-3N matrix, defined as:

$$[H] = \begin{bmatrix} [I_3] & [O_3] & & & & & & & \\ B_c[I_3] & A_c[I_3] & B_c[I_3] & & & & & & \\ & \ddots & \ddots & \ddots & & & & & \\ & & B_c[I_3] & A_c[I_3] & B_c[I_3] & & & & \\ & & & [O_3] & [I_3] & [O_3] & & & \\ & & & & B_c[I_3] & A_c[I_3] & B_c[I_3] & & \\ & & & & & \ddots & \ddots & \ddots & \\ & & & & & & B_c[I_3] & A_c[I_3] & B_c[I_3] \\ & & & & & & & [O_3] & [I_3] \end{bmatrix} \begin{matrix} IP_1 \\ IP_2 \\ \vdots \\ IP_{j-1} \\ IP_j \\ IP_{j+1} \\ \vdots \\ IP_{N-1} \\ IP_N \end{matrix} \qquad (22)$$

367 where $[I_3]$ and $[O_3]$ are 3-by-3 identity and zero matrices, respectively, and A_c and B_c are con-

368 stants, determined as:

$$A_c = 1 + \left(\frac{l_c}{\Delta x}\right)^2 \quad \text{and} \quad B_c = -\frac{1}{2}\left(\frac{l_c}{\Delta x}\right)^2 \qquad (23)$$

369 Utilizing Eq. (21), Eqs. (19) can be condensed in the following matrix form:

$$\begin{cases} [B_Q]\vec{Q} - \vec{F}_{ms}\left(\vec{d}_{tot}^e\right) = \vec{0} \\ [b_{fr}]\vec{Q} - f_{fr}\left(u_{sl}, k_{fr}, \mu\sigma(x_j, y)\right) = \vec{0} \\ \vec{q} - [B_q][H]^{-1}\vec{d}_{tot}^e - [b_{fr}]^T u_{sl} = \vec{0} \end{cases} \qquad (24)$$

370 with:

$$
\left[B_Q \right] =
\begin{bmatrix}
\left[b(x_1) \right] \\
\left[b(x_2) \right] \\
\vdots \\
\left[b(x_N) \right]
\end{bmatrix}_{3N \times 3}
\quad , \quad
\vec{F}_{ms} \left(\vec{d}^{\,e}_{tot} \right) =
\begin{Bmatrix}
\vec{f}_{ms} \left(\vec{d}^{\,e}(x_1) \right) \\
\vec{f}_{ms} \left(\vec{d}^{\,e}(x_2) \right) \\
\vdots \\
\vec{f}_{ms} \left(\vec{d}^{\,e}(x_N) \right)
\end{Bmatrix}_{3N \times 1}
\tag{25}
$$

$$
\left[B_q \right] = \left[w_1 \left[b(x_1) \right]^T \quad w_2 \left[b(x_2) \right]^T \quad \cdots \quad w_N \left[b(x_N) \right]^T \right]_{3 \times 3N}
$$

371 where $\vec{F}_{ms}$ is the vector including the section forces at all IP locations, $\left[B_Q \right]$ is the discretized force

372 shape function matrix, and $\left[B_q \right]$ is the matrix of integration weights. The final system of equations

373 (Eqs. (24)) can be solved by using Newton-Raphson iterative solution algorithm, as:

$$
\begin{Bmatrix}
\vec{Q} \\
u_{sl} \\
\vec{d}^{\,e}_{tot}
\end{Bmatrix}_{k+1}
=
\begin{Bmatrix}
\vec{Q} \\
u_{sl} \\
\vec{d}^{\,e}_{tot}
\end{Bmatrix}_{k}
-
\begin{bmatrix}
\left[B_Q \right]_{3N \times 3} & [0]_{3N \times 1} & -\left[K_{ms} \right]_{3N \times 3N} \\
\left[b_{fr} \right]_{1 \times 3} & -K_{fr} & [0]_{1 \times 3N} \\
[0]_{3 \times 3} & -\left[b_{fr} \right]^T_{3 \times 1} & -\left[B_q \right][H]^{-1}_{3 \times 3N}
\end{bmatrix}^{-1}_{k}
\begin{Bmatrix}
\left[B_Q \right]\vec{Q} - \vec{F}_{ms} \left(\vec{d}^{\,e}_{tot} \right) \\
\left[b_{fr} \right]\vec{Q} - f_{fr} \left(u_{sl}, ... \right) \\
\vec{q} - \left[B_q \right][H]^{-1} \vec{d}^{\,e}_{tot} - \left[b_{fr} \right]^T u_{sl}
\end{Bmatrix}_{k}
\tag{26}
$$

374 where k is the iteration number, and $\left[K_{ms} \right]$ is the matrix including tangent section stiffness matrices

375 (for all IP locations) on its diagonal, as:

$$
\left[K_{ms} \right] =
\begin{bmatrix}
\left[k_{ms}(x_1) \right] & [0] & \cdots & [0] \\
[0] & \left[k_{ms}(x_2) \right] & \cdots & [0] \\
\vdots & \vdots & & \vdots \\
[0] & [0] & \cdots & \left[k_{ms}(x_N) \right]
\end{bmatrix}
\tag{27}
$$

376 The element tangent flexibility matrix (Eq. (17)) can be computed as:

$$
\left[f_{el} \right] = \frac{\partial \vec{q}}{\partial \vec{Q}} = \left[B_q \right] \left[K_{ms} \right]^{-1} \left[B_Q \right] + \left[b_{fr} \right]^T K_{fr}^{-1} \left[b_{fr} \right]
\tag{28}
$$

HSR Column Modeling Strategy using the HSR Element

378 The proposed HSR element formulation was implemented in the structural analysis program Open-
379 Sees (McKenna et al. 2000) by the authors and utilized here. Because each HSR element includes
380 only one sliding-rocking joint, modeling of HSR columns with the HSR element formulation re-
381 quires use of one HSR element per joint. For all, except for the bottom joint, the first node of the
382 HSR element should be located within the segment prior to the HSR joint, while the second node
383 of the element should be located within the segment after the HSR joint. Thus, the sliding-rocking
384 joint of the HSR element formulation is placed within the element length, at a location representing
385 the physical location of the HSR joint. For the bottom joint, the first node of the HSR element
386 should be located at the lower end of the bottom segment, because the foundation is typically
387 considered rigid, while the second node of the HSR element should be located within the bottom
388 segment above the joint. In this case, the sliding-rocking joint is placed at the first/lower node of
389 the HSR element, i.e. the physical location of the HSR joint. Application of this modeling strategy
390 is demonstrated in Fig. 6 for the HSR column from the studies by Sideris et al. (2014b); (2014c).
391 The interior part of each precast segment is modeled by a GI FB beam-column element connected

392   to two HSR elements at the segment ends. The length of the HSR elements is selected such that
393   their end nodes are located at the ends of the duct adaptors in order to ensure that bearing forces
394   applied to the duct adaptors are properly transferred to the segment via "rigid" links. "Rigid" links
395   are modeled by linear elastic beam elements of high stiffness. Each tendon is modeled by a set of
396   corotational truss elements, the lateral displacement of which is constrained to remain within the
397   ducts and duct adaptors by zero-length gap elements oriented horizontally. These gap elements are
398   connected to the HSR element ends through "rigid" links allowing transfer of the tendon bearing
399   forces to the segments. For the material model of the tendons, a tension-only uniaxial model fol-
400   lowing Mattock's backbone curve (Mattock 1979) and incorporating linear loading/unloading and
401   damage through a strain-dependent damage reduction factor (Sideris et al. 2014a) was imple-
402   mented in OpenSees by the authors. The damage reduction factor is used to simulate potential
403   tendon fracture. Initial post-tensioning is simulated by assigning an initial strain to the tendon
404   material model.

405   ### *Evaluation*

406   The proposed modeling strategy using the developed HSR element formulation is employed to
407   simulate two large-scale experiments conducted at the University at Buffalo (Sideris 2012; Sideris
408   et al. 2014b; c): a quasi-static test on a single-column HSR pier, and a shake table test on a bridge
409   with two single-column HSR piers. The HSR column specimens (Fig. 7) consisted of five precast
410   concrete segments, a cap-beam and a foundation block, which were post-tensioned together with
411   eight internal unbonded tendons. The tendons were seven-wire monostrands conforming to Gr.
412   270 per ASTM A416/A416M (2010) with a diameter of 0.6 in [1.52 cm]. The ducts had a diameter
413   of 0.9 in. [2.27 cm], while the duct adaptors, used at both ends of the column segments, had interior
414   diameter of 1.375 in. [3.49 cm] and height of 1.5 in. [3.81 cm]. No duct adaptors were used in the
415   cap beam and the foundation block. All HSR joints included a thin layer of silicone material (OSI
416   HM-270 2011) to achieve a target coefficient of friction of 0.08 to 0.1 (Sideris 2012; Sideris et al.
417   2014c). The 28-day nominal strength of the concrete material was 5 ksi [34.5 MPa], while the mild
418   reinforcing steel conformed to Gr. 60 per ASTM A615/A615M (2009). The longitudinal mild re-
419   inforcement of the column segments was comprised of #3 straight bars that provided a volumetric
420   ratio of 0.025. The transverse reinforcement of the column segments consisted of #3 closed ties in
421   each wall, providing volumetric reinforcement ratios of 0.0198 and 0.014 in the wall-parallel and
422   wall-normal directions, respectively.
423   All analyses are conducted in two dimensions considering excitation and response in the lateral
424   and vertical directions. The column cross-section is discretized into fibers/layers of approximate
425   width of 0.625 in [1.59 cm], as demonstrated in Fig. 8. The stress-strain backbone curves consid-
426   ered for the different materials are shown in Fig. 9 (a-c). The constitutive model by Mattock (1979)
427   for the PT tendon is calibrated in accordance with Sideris et al. (2014a). For the mild reinforcing
428   steel, the Giuffré-Menegotto-Pinto model (Giuffrè and Pinto 1970) is used with a strain hardening
429   ratio of 0.01, while the confined and unconfined concrete are simulated using the modified Kent
430   and Park model (Scott et al. 1982). Based on the test data from Sideris (2012), the measured
431   strength of the unconfined concrete was 5.7 ksi [39.3 MPa], while the estimated strength and ulti-
432   mate strain of the confined concrete were 7.75 ksi [53.4 MPa] and 0.0041, respectively (Sideris et
433   al. 2014c). At the HSR joints, all material models used for the cross-section fibers have zero tensile
434   strength. The hysteretic friction model of Eq. (7) is considered at all individual cross-section fibers,
435   while the variation of coefficient of friction with the contact pressure/stress is considered in ac-
436   cordance with the exponential law shown in Fig. 9 (d) based on the test data and calibration by

437 Sideris (2012). The force reaction of the gap elements between the tendons and ducts or duct adap-
438 tors is zero prior to engaging the gap, and increases linearly (with high stiffness) with the gap
439 "violation". Inelasticity or damage at the contact of ducts and duct adaptors is not considered.

440 **Simulation of Quasi-Static Response of HSR Column**

441 The quasi-static test setup is shown in Fig. 10. In this test, the initial post-tensioning load was 20
442 kips [89 kN] per tendon. The total gravity load of 44 kips [196 kN] was applied through two
443 external tendons, each having a PT force of 18 kips [80 kN], and by the weight of the actuators
444 together with the connection setup (8 kips [36 kN]). The test specimen was subjected to a displace-
445 ment-controlled lateral loading protocol, including symmetric double cycles of increasing ampli-
446 tude. The peak drift ratio was 14.9%.

447 In the generated model, the gravity tendons are simulated by truss elements, while the weight
448 of the actuators and the lateral load are applied at the location of the swivel, as shown in Fig. 11.
449 The distance of the swivel from the column centerline is estimated to be 30 in. [76.2 cm]. The HSR
450 column itself is modeled as described above and shown in Fig. 7.

451 Comparisons between computational and experimental data in terms of the lateral force vs.
452 lateral displacement response and the total PT force vs. lateral displacement response are shown
453 in Fig. 12 (a) and (b), respectively. The model accurately predicts the lateral strength in both di-
454 rections, including the softening observed with the increasing displacement amplitudes. However,
455 residual displacements are underestimated for cycles with larger displacement amplitudes. This
456 underestimation is due to drops in the lateral force upon displacement/load reversals indicative of
457 friction-type effects, which are not captured by the model. The cause of those drops is still unde-
458 termined; consideration of two potential causes, namely, the friction between the tendons and the
459 ducts/duct adaptors, and the friction in the actuator swivels, have not been found to significantly
460 improve the predictions. However, as shown later, such friction-type drops did not appear in the
461 shake table tests.

462 The model accurately predicted residual post-tensioning forces (Fig. 12 (b)); however, it over-
463 estimated peak PT forces by 20%. This overestimation of the peak PT forces resulted from the
464 larger rocking rotation demands at the bottom in the model (Fig. 12 (c)**Error! Reference source
465 not found.**), due to the smaller joint sliding amplitudes predicted by the model under large applied
466 displacements (Fig. 13), and from the slightly larger moment reaction at the bottom joint compared
467 to those measured during the test (Fig. 12 (c)**Error! Reference source not found.**). A comparison
468 of computational and experimental joint shear vs. sliding responses, for all HSR joints, is shown
469 in Fig. 13. The model demonstrates the capability of simulating joint sliding; however, peak sliding
470 is underestimated, because bearing concrete damage caused by the PT tendons at the connection
471 between ducts and duct adaptors (Sideris 2012) is not simulated. Moreover, during the actual test,
472 concrete compressive damage at the bottom joint introduced significant debris at the sliding inter-
473 face, resulting in a different sliding behavior compared to the joints above, which was difficult to
474 accurately capture by the HSR element. Due to the uncertainty in the frictional properties intro-
475 duced by such debris, Sideris et al. (2014c) recommended that sliding should always be restrained
476 in the end rocking joints.

477 **Simulation of Shake Table Test on HSR Bridge**

478 The shake table test setup is shown in Fig. 14. The superstructure was simply supported on the
479 cap-beams through simple contact, and sliding was prevented via dry concrete-to-concrete friction.
480 The bridge specimen – including several variations (Sideris et al. 2015) – was subjected to nearly
481 145 tests. For the test considered (ABC_S1_SC_M2_YZ, per Sideris 2012), the input motion was
482 the base excitation from the 1979 Imperial Valley earthquake, recorded at the Delta station. The

483 horizontal components of the originally recorded motion were scaled to represent 2.4 times the
484 maximum considered earthquake (MCE) hazard level, while the vertical component was scaled to
485 represent 3.6 times the MCE hazard level. The initial post-tensioning load prior to this test was
486 almost 15 kips [67 kN] per tendon.
487 In accordance with this test, the simulation is conducted using the lateral and vertical ground
488 motion components (y-z directions, per Fig. 14) and using one out of the two HSR piers supporting
489 half of the superstructure weight. The superstructure-to-cap-beam connectivity is represented by
490 two HSR elements (Fig. 15), while the superstructure's seismic mass and mass moment of inertia
491 are assigned to a node located at the centroid of the superstructure cross section (Fig. 15). To
492 maintain consistency with the experimental response, the dynamic analysis is performed using the
493 acceleration time histories recorded on the shake table (Fig. 16). The damping forces are computed
494 using the Rayleigh method, assigning a damping ratio of 3% to the first and the second modes of
495 vibration. This value of the damping ratio is smaller than the values reported by Sideris et al.
496 (2015), which also accounted for small joint sliding (hysteretic energy dissipation) activated dur-
497 ing white noise tests (Sideris 2012).
498 The lateral displacement of the superstructure relative to the foundation obtained from the anal-
499 ysis is compared with the corresponding experimental data in Fig. 17. The analysis predictions are
500 in good agreement with the test data, both in terms of peak amplitudes and frequency content. The
501 peak positive displacement obtained from the analysis is only 5% less than the corresponding ex-
502 perimental value, while the peak negative displacement is almost identical to the corresponding
503 experimental value. The predicted residual displacement is almost zero, in accordance with the
504 experimental data. However, towards the end of the motion, the experimental response has larger
505 displacement amplitude and decays more slowly than the simulated response, which has much
506 smaller displacements and decays more rapidly. This response results from the accumulated dam-
507 age at the bottom joint during prior testing, which cannot be captured by this analysis, which only
508 considers a single motion and starts from undamaged conditions.
509 The column base shear vs. lateral displacement at the cap beam obtained from the test and the
510 analysis are in good agreement (Fig. 18 (a)) in terms of the predicted peak base shear and peak
511 displacement. However, the test specimen is more flexible (in the elastic range), because of the
512 accumulated damage at the bottom joint during prior testing. As a result, the model accurately
513 captures, both in terms of peak responses and frequency content, the portion of the system response
514 associated with the large joint sliding and rocking (i.e., first 35 seconds in Fig. 17) driven by the
515 high intensity part of the applied ground motion (Fig. 16). However, it does not capture the (flex-
516 ible) elastic response towards the end of the motion (i.e., between 45 and 55 seconds in Fig. 17),
517 because the accumulated stiffness deterioration from prior testing is not accounted for in the sim-
518 ulation. This is also demonstrated by a comparison of the period of the first lateral (cantilever-like)
519 mode, which was 0.36 sec for the test specimen prior to this test, as opposed to 0.28 sec. predicted
520 by the model. In addition, the predicted peak PT forces are up to 20% larger than the peak PT
521 forces recorded during testing (Fig. 18 (b)), which is consistent with the stiffer behavior of the
522 simulated column (Fig. 18 (a)).
523 The joint shear vs. sliding responses obtained from the analysis for the three instrumented joints
524 (joints 0, 1 and 5 per Fig. 7) match the corresponding experimental responses reasonably well (Fig.
525 19). The peak sliding displacements recorded through the simulation closely resemble those meas-
526 ured during the test, but the simulation overestimated the peak negative joint sliding at the second
527 from the bottom joint (joint 1). The simulation also predicted that, under dynamic loading, only
528 the two lower joints undergo considerable sliding, while the third joint from the bottom exhibits

529 minor sliding, which is in agreement with experimental observations (Sideris 2012). These results
530 also suggest that similar seismic performance may be achieved by a smaller number of sliding
531 joints since the upper joints did not slide.

Summary and Conclusions

533 This study introduces a novel two-node HSR element formulation that is capable of capturing the
534 response properties of members with HSR joints, thereby allowing simulation of the dynamic re-
535 sponse of bridges with HSR columns. The proposed formulation addresses deficiencies in existing
536 models by combining (*i*) a gradient inelastic beam theory (Sideris and Salehi 2016; Salehi and
537 Sideris 2017), which can simulate member material deformations and joint rocking through com-
538 pression-only section constitutive relations at the location of the HSR joint, with (*ii*) a pressure-
539 dependent hysteretic friction model, capable of simulating joint sliding. The proposed HSR ele-
540 ment is implemented in the structural analysis software OpenSees (McKenna et al. 2000) and used
541 in the framework of a proposed modeling strategy to simulate the response of HSR columns. Two
542 past experimental studies are considered, including quasi-static testing of an HSR column, and
543 shake table testing of a bridge with two single-column HSR piers. Major findings include:

544 • The proposed HSR element formulation and modeling strategy were capable of simulating the
545 fundamental response mechanisms of HSR columns, namely, the sliding-rocking interac-
546 tions/responses at HSR joints, and interactions between the unbonded tendons and concrete
547 segments in the vicinity of the duct adaptors. The HSR element formulation eliminated strain
548 localization and loss of objectivity, present in other rocking-type models. Also, analyses with
549 the HSR element avoided *chattering* (i.e., high frequency fluctuations in the numerical solu-
550 tion) and eventual convergence failure of the solution algorithm, phenomena that often occur
551 in structural models incorporating two-node contact sliders distributed over the cross-section
552 and subjected to large rapid variation of the contact pressure (as is the case for HSR joints).
553 Alleviation of chattering was achieved because, in the proposed HSR element formulation,
554 large rapid variations of the contact normal stresses at individual fibers over the cross-section
555 (e.g., due to rapid softening of edge fibers) result in significantly smaller/smoother temporal
556 variation of the cross-section resultant forces (axial, shear, moment) obtained via integration
557 of cross-section stresses over the cross-section area. On the contrary, large rapid variations in
558 the force of the individual two-node contact sliders are directly incorporated in the dynamic
559 structural equilibrium equations, causing instabilities in the numerical temporal solution.

560 • Under quasi-static loading, the model accurately predicted the peak lateral strength (including
561 softening) at all displacement amplitudes. However, residual deformations were underesti-
562 mated, mostly because of a friction-type contribution from undetermined sources that appeared
563 upon load reversal during cycles of large displacement amplitudes and was not captured by the
564 proposed modeling strategy. Such friction-type contributions were not observed during dy-
565 namic testing, for which the proposed modeling strategy provided more accurate results in
566 terms of peak lateral strength and displacement, joint sliding demands, and residual defor-
567 mations.

568 • In accordance with the experimental data, the model predicted that joint sliding was limited to
569 the lower joints, implying that similar responses can be obtained with fewer HSR joints over
570 the column height. From a design perspective, this observation can result in more cost-effective
571 designs.

572 • Concrete damage at the bottom (rocking) joint introduced significant debris at the sliding in-
573 terface, making the frictional sliding response at that joint difficult to predict. This observation

574 also validated the design recommendation from Sideris et al. (2014c), which advocated for
575 restraining sliding at the end rocking joints.

576 The capability to accurately simulate the response of bridges incorporating HSR columns will
577 enable examination of design decisions, including the number and distribution of HSR joints, duct
578 adaptor size, coefficient of friction, and other features, which will facilitate the development of
579 HSR bridge designs for high seismicity regions.

Acknowledgments

References

585 Abdelkarim, O. I., ElGawady, M. A. (2014). "Analytical and Finite-Element Modeling of FRP-
586 Concrete-Steel Double-Skin Tubular Columns." *Journal of Bridge Engineering*.
587 Ameli, M. J., Pantelides, C. P. (2016). "Seismic Analysis of Precast Concrete Bridge Columns
588 Connected with Grouted Splice Sleeve Connectors." *Journal of Structural Engineering*,
589 0(0): 04016176, DOI: doi:10.1061/(ASCE)ST.1943-541X.0001678.
590 <http://ascelibrary.org/doi/abs/10.1061/%29ASCE%29ST.1943-541X.0001678>.
591 ASTM A416/A416M (2010). *Standard Specification for Steel Strand, Uncoated Seven-Wire for
592 Prestressed Concrete*, ASTM International, West Conshohocken, PA, U.S.A.
593 ASTM A615/A615M (2009). *Standard Specification for Deformed and Plain Carbon-Steel Bars
594 for Concrete Reinforcement*, ASTM International, West Conshohocken, PA, U.S.A.
595 Billington, S. L., Yoon, J. (2004). "Cyclic response of unbonded posttensioned precast columns
596 with ductile fiber-reinforced concrete." *Journal of Bridge Engineering*, 9(4): 353-363.
597 Bu, Z., Guo, J., Zheng, R., Song, J., Lee, G. C. (2016). "Cyclic performance and simplified
598 pushover analyses of precast segmental concrete bridge columns with circular section."
599 *Earthquake Engineering and Engineering Vibration*, 15(2): 297-312, DOI:
600 10.1007/s11803-016-0323-3. <http://dx.doi.org/10.1007/s11803-016-0323-3>.
601 Coleman, J., Spacone, E. (2001). "Localization Issues in Force-Based Frame Elements." *Journal
602 of Structural Engineering*, 127(11): 1257-1265.
603 CSI (2009). *CSI Analysis Reference Manual for SAP200, ETABS, SAFE and CSiBridge*,
604 Computers and Structures Inc. (CSI), Berkeley, CA, USA
605 Dawood, H., ElGawady, M., Hewes, J. (2011). "Behavior of Segmental Precast Posttensioned
606 Bridge Piers under Lateral Loads." *Journal of Bridge Engineering*, 17(5): 735-746.
607 Dawood, H. M., ElGawady, M. (2013). "Performance-based Seismic Design of Unbonded Precast
608 Post-tensioned Concrete Filled GFRP Tube Piers." *Composites Part B: Engineering*, 44(1):
609 357-367.
610 DS (2010). *ABAQUS*, Dassault Systèmes, Providence, RI, USA
611 ElGawady, M. A., Dawood, H. M. (2012). "Analysis of Segmental Piers consisted of Concrete
612 Filled FRP tubes." *Engineering Structures*, 38: 142-152.
613 Figg, L., Pate, W. D. (2004). "Precast concrete segmental bridges-America's beautiful and
614 affordable icons." *Precast/Prestressed Concrete Institute (PCI) Journal*, 49(5): 26-38.
615 Freyermuth, C. L. (1999). " Ten Years of Segmental Achievements and Projections for the Next
616 Century." *Precast/Prestressed Concrete Institute (PCI) Journal*, 44(3): 36-44.
617 Giuffrè, A., Pinto, P. E. (1970). "Il comportamento del cemento armato per sollecitazioni cicliche
618 di forte intensità." *Giornale del Genio Civile*, 5(1): 391-408.

619 Guerrini, G., Restrepo, J. I., Massari, M., Vervelidis, A. (2014). "Seismic Behavior of
620   Posttensioned Self-Centering Precast Concrete Dual-Shell Steel Columns." *Journal of*
621   *Structural Engineering*.
622 Haraldsson, O. S., Pang, J. B. K., Stanton, J. F., Eberhard, M. O. (2009). "A Precast Concrete
623   Bridge Bent for Seismic Regions." *Proceedings of the Special International Workshop on*
624   *Seismic Connection Details for Segmental Bridge Construction - Technical Report*
625   *MCEER-09-0012*, Seattle, Washington, July 22-24, Multidisciplinary Center for
626   Earthquake Engineering Research, Buffalo, NY, U.S.A.
627 Haraldsson, O. S., Janes, T. M., Eberhard, M. O., Stanton, J. F. (2013). "Seismic Resistance of
628   Socket Connection between Footing and Precast Column." *Journal of Bridge Engineering*,
629   18(9): 910-919.
630 Hewes, J. T., Priestley, M. J. N. (2002). "Seismic Design and Performance of Precast Concrete
631   Segmental Bridge Columns." Report No. SSRP–2001/25, Department of Structural
632   Engineering, University of California, San Diego, La Jolla, California 92093-0085,
633 Hewes, J. T. (2007). "Seismic Tests on Precast Segmental Concrete Columns with Unbonded
634   Tendons." *Bridge Structures: Assessment, Design and Construction*, 3(3): 215 - 227.
635   <http://www.informaworld.com/10.1080/15732480701520352>.
636 Ichikawa, S., Matsuzaki, H., Moustafa, A., ElGawady, M. A., Kawashima, K. (2016). "Seismic-
637   Resistant Bridge Columns with Ultrahigh-Performance Concrete Segments." *Journal of*
638   *Bridge Engineering*: 04016049.
639 Kurama, Y., Pessiki, S., Sause, R., Lu, L.-W. (1999). "Seismic Behavior and Design of Unbonded
640   Post-Tensioned Precast Concrete Walls." *PCI Journal*, 44(3): 72-89.
641 Lee, W., Jeong, H., Billington, S., Mahin, S., Sakai, J. "Post-Tensioned Structural Concrete Bridge
642   Piers with Self-Centering Characteristics." *Proc., Structures Congress 2007*, ASCE, 1-15.
643 Lehman, D. E., Roeder, C. W. (2012). "Foundation connections for circular concrete-filled tubes."
644   *Journal of Constructional Steel Research*, 78: 212-225.
645 Madhusudhanan, S., Sideris, P. (2015). "Direct Displacement-Based Seismic Design and
646   Validation for Hybrid Sliding-Rocking Bridge Substructure Systems." *Structures Congress*
647   *2015*, 497-513, <http://ascelibrary.org/doi/abs/10.1061/9780784479117.044>
648 Mander, J. B., Cheng, C.-T. (1997). "Seismic design of bridge piers based on damage avoidance
649   design (NCEER-97-0014)." National Center for Earthquake Engineering Research,
650   Buffalo, N.Y.,
651 Marriott, D., Pampanin, S., Palermo, A. (2009). "Quasi-static and Pseudo-dynamic Testing of
652   Unbonded Post-tensioned Rocking Bridge Piers with External Replaceable Dissipaters."
653   *Earthquake Engineering & Structural Dynamics*, 38(3): 331-354, DOI: 10.1002/eqe.857.
654   <http://dx.doi.org/10.1002/eqe.857>.
655 Marsh, M. L., Wernli, M., Garrett, B. E., Stanton, J. F., Eberhard, M. O., Weinert, M. D. (2011).
656   "NCHRP Report 698: Synthesis on System Performance of Accelerated Bridge
657   Construction Connections in Moderate-to-High Seismic Regions." NCHRP 12-88,
658   National Cooperative Highway Research Program (NCHRP), Transportation Research
659   Board of National Academies,
660 Matsumoto, E. E., Waggoner, M. C., Kreger, M. E., Vogel, J., Wolf, L. (2008). "Development of
661   a Precast Concrete Bent-Cap System." *PCI Journal*, 53(3): 74-99.
662 Mattock, A. H. (1979). "Flexural Strength of Prestressed Concrete Sections by Programmable
663   Calculator." *PCI Journal*, 24(1): 32-54.
664 McKenna, F., Fenves, G. L., Scott, M. H. (2000). "*Open System for Earthquake Engineering*

Simulation", Version 2.2.2, Pacific Earthquake Engineering Research Center, Berkeley, CA, USA.

Motaref, S., Saiidi, M., Sanders, D. (2014). "Shake Table Studies of Energy Dissipating Segmental Bridge Columns." *Journal of Bridge Engineering*, 19(3): 186-199, DOI: 10.1061/(ASCE)BE.1943-5592.0000518. <http://ascelibrary.org/doi/abs/10.1061/%28ASCE%29BE.1943-5592.0000518>.

Nikoukalam, M. T., Sideris, P. (2016). "Low-Damage Post-Tensioned Segmental Bridge Columns with Flexible End Joints for Seismic Accelerated Bridge Construction." *Transportation Research Record (TRR) - Journal of the Transportation Research Board - Structures*, DOI: http://dx.doi.org/10.3141/2592-17.

Nikoukalam, M. T., Sideris, P. (2017). "Resilient Bridge Rocking Columns with Polyurethane Damage-Resistant End Segments and Replaceable Energy Dissipating Links." *ASCE Journal of Bridge Engineering (Accepted)*.

OSI HM-270 (2011). "Construction Silicone Sealant." Henkel Corporation, <http://www.osipro.com/products.pl?id=HM-270 >. (Accessed in 2011).

Ou, Y.-C., Tsai, M. S., Chang, K. C., Lee, G. C. (2010a). "Cyclic behavior of precast segmental concrete bridge columns with high performance or conventional steel reinforcing bars as energy dissipation bars." *Earthquake Engineering & Structural Dynamics*, 39(11): 1181-1198, DOI: 10.1002/eqe.986. <http://dx.doi.org/10.1002/eqe.986>.

Ou, Y.-C., Wang, P.-H., Tsai, M.-S., Chang, K.-C., Lee, G. C. (2010b). "Large-Scale Experimental Study of Precast Segmental Unbonded Posttensioned Concrete Bridge Columns for Seismic Regions." *Journal of Structural Engineering*, 136(3): 255-264. <http://dx.doi.org/10.1061/(ASCE)ST.1943-541X.0000110>.

Palermo, A., Pampanin, S., Carr, A. (2005). "Efficiency of Simplified Alternative Modeling Approaches to Predict the Seismic Response of Precast Concrete Hybrid Systems." *fib Symposium "Keep Concrete Attractive"*, Budapest, Hungary, International Federation for Structural Concrete (*fib*)

Pang, J. B., Eberhard, M. O., Stanton, J. F. (2010). "Large-Bar Connection for Precast Bridge Bents in Seismic Regions." *Journal of Bridge Engineering*, 15(3): 231-239.

Pantelides, C. P., Ameli, M. J., Parks, J. E., Brown, D. N. (2014). "Seismic Evaluation of Grouted Splice Sleeve Connections for Precast RC Bridge Piers in ABC." UT- 14.09, Department of Civil and Environmental Engineering, University of Utah, Salt Lake City, Utah 84112

Perez, F. J., Sause, R., Pessiki, S. (2007). "Analytical and Experimental Lateral Load Behavior of Unbonded Posttensioned Precast Concrete Walls." *Journal of Structural Engineering*, 133(11): 1531-1540.

Restrepo, J. I., Tobolski, M. J., Matsumoto, E. E. (2011). "NCHRP Report 681: Development of a Precast Bent Cap System for Seismic Regions." NCHRP 12-74, National Cooperative Highway Research Program (NCHRP), Transportation Research Board of National Academies,

Roh, H. (2007). "Seismic Behavior of Structures Using Rocking Columns and Viscous Dampers." Ph.D., Department of Civil, Structural and Environmental Engineering, State University of New York at Buffalo.

Roh, H., Reinhorn, A. M. (2010). "Nonlinear Static Analysis of Structures with Rocking Columns." *Journal of Structural Engineering*, 136(5): 532-542.

Salehi, M., Sideris, P. (2016). "Nonlinear Dynamic Analysis of Hybrid Sliding-Rocking Bridges." *Geotechnical and Structural Engineering Congress 2016*, Phoenix, AZ, USA, 90-102,

ASCE

Salehi, M., Sideris, P. (2017). "Refined Gradient Inelastic Flexibility-Based Formulation for Members Subjected to Arbitrary Loading." *Journal of Engineering Mechanics (Accepted)*.

Salehi, M., Sideris, P., Liel, A. (2017). "Seismic Collapse Analysis of RC Framed Structures using the Gradient Inelastic Force-Based Element Formulation." *16th World Conference on Earthquake Engineering (16WCEE)*, Santiago Chile, January 9 - 13,

Scott, B. D., Park, R., Priestley, M. J. N. (1982). "Stress-Strain Behavior of Concrete Confined by Overlapping Hoops at Low and High Strain Rates." *Journal of the American Concrete Institute*, 79(1): 13-27.

Shen, Q., Kurama, Y., Weldon, B. D. (2006). "Seismic Analysis, Behavior, and Design of Unbonded Post-Tensioned Hybrid Coupled Wall Structures." University of Notre Dame, Notre Dame, IN, USA

Shrestha, K. C., Saiidi, M. S., Cruz, C. A. (2015). "Advanced materials for control of post-earthquake damage in bridges." *Smart Materials and Structures*, 24(2): 025035.

Sideris, P., Anagnostopoulou, M., Aref, A. J., Filiatrault, A. "Seismic Performance of Precast Segmental Bridges." *Proc., The 9th U.S. National and 10th Canadian Conference on Earthquake Engineering*.

Sideris, P. (2012). "Seismic Analysis and Design of Precast Concrete Segmental Bridges." Ph.D., Department of Civil, Structural, and Environmental Engineering, University at Buffalo, Buffalo, NY, USA.

Sideris, P., Aref, A. J., Filiatrault, A. (2014a). "Effects of Anchorage Hardware on the Cyclic Tensile Response of Unbonded Monostrands." *PCI Journal*, 59(6): 60-77. <http://www.pci.org/uploadedFiles/Siteroot/Publications/PCI_Journal/2014/DOI_Articles/JL-14_Summer9.pdf >.

Sideris, P., Aref, A. J., Filiatrault, A. (2014b). "Large-Scale Seismic Testing of a Hybrid Sliding-Rocking Posttensioned Segmental Bridge System." *Journal of Structural Engineering*, 140(6).

Sideris, P., Aref, A. J., Filiatrault, A. (2014c). "Quasi-Static Cyclic Testing of a Large-Scale Hybrid Sliding-Rocking Segmental Column with Slip-Dominant Joints." *Journal of Bridge Engineering*, 19(10).

Sideris, P., Aref, A. J., Filiatrault, A. (2015). "Experimental Seismic Performance of a Hybrid Sliding–Rocking Bridge for Various Specimen Configurations and Seismic Loading Conditions." *Journal of Bridge Engineering*, 20(11).

Sideris, P. (2015). "Nonlinear Quasi-Static Analysis of Hybrid Sliding–Rocking Bridge Columns Subjected to Lateral Loading." *Engineering Structures*, 101: 125-137.

Sideris, P., Salehi, M. (2016). "A Gradient-Inelastic Flexibility-based Frame Element Formulation." *Journal of Engineering Mechanics*, 142(7): 04016039, DOI: 10.1061/(ASCE)EM.1943-7889.0001083.

Spieth, H. A., Carr, A. J., Murahidy, A. G., Arnolds, D., Davies, M., Mander, J. B. (2004). "Modelling of Post-Tensioned Precast Reinforced Concrete Frame Structures with Rocking Beam-Column Connections." *2004 NZSEE Conference*, Auckland, New Zealand, New Zealand Society for Earthquake Engineering Inc.

Tazarv, M., Saiidi, M. S. (2013). "Emulative Moment-Resistant RC Bridge Column-Footing Connection for Accelerated Bridge Construction in High Seismic Zone." *7th National Seismic Conference on Bridges & Highways*, Oakland, CA, U.S.A.,

Wang, Z., Song, W., Wang, Y., Wei, H. (2011). "Numerical Analytical Model for Seismic

757   Behavior of Prestressing Concrete Bridge Column Systems." *The Twelfth East Asia-Pacific*
758   *Conference on Structural Engineering and Construction*, Hong Kong, China, Elsevier
759 Weinert, M. D. (2011). "Substructure Connections for accelerated bridge construction in seismic
760   regions." M.Sc. Thesis, Department of Civil and Environmental Engineering, University
761   of Washington, Seattle, WA.
762 White, S. L. (2014). "Controlled Damage Rocking Systems for Accelerated Bridge Construction."
763   M.Eng., Department of Civil and Natural Resource Engineering, University of Canterbury.
764
765
766
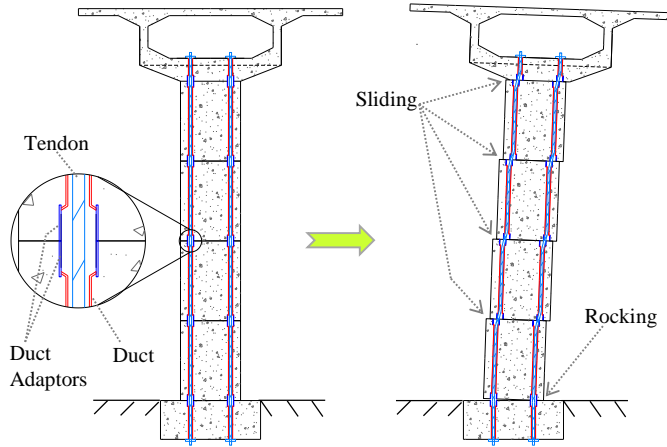
769
770 **Fig. 1. Substructure column of HSR bridges, showing rocking and sliding behavior of the HSR joints as anticipated**
771 **in design**

772
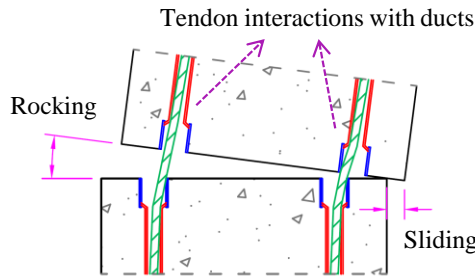
773
774 **Fig. 2. Behavior of joints in HSR column, illustrating simulation challenges**

775
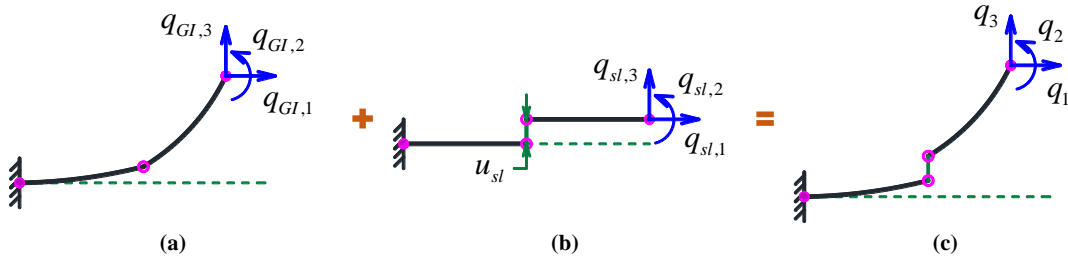
776 **(a)** **(b)** **(c)**
777 **Fig. 3. Displacement decomposition for HSR element: (a) displacements due to material deformations and joint**
778 **rocking, $\vec{q}_{GI}$, accounted for by GI FB element formulation; (b) displacements due to joint sliding, $\vec{q}_{sl}$, accounted**
779 **for by hysteretic friction model; and (c) total displacements, $\vec{q}$.**

780
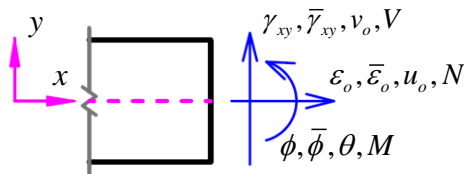
781
782 **Fig. 4. Section strains, displacements, and forces**

1

783
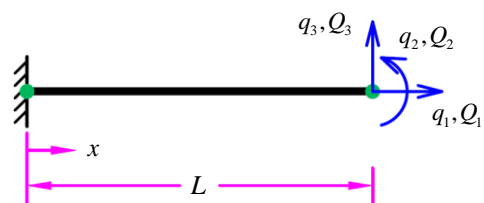
Fig. 5. Cantilever reference system

786
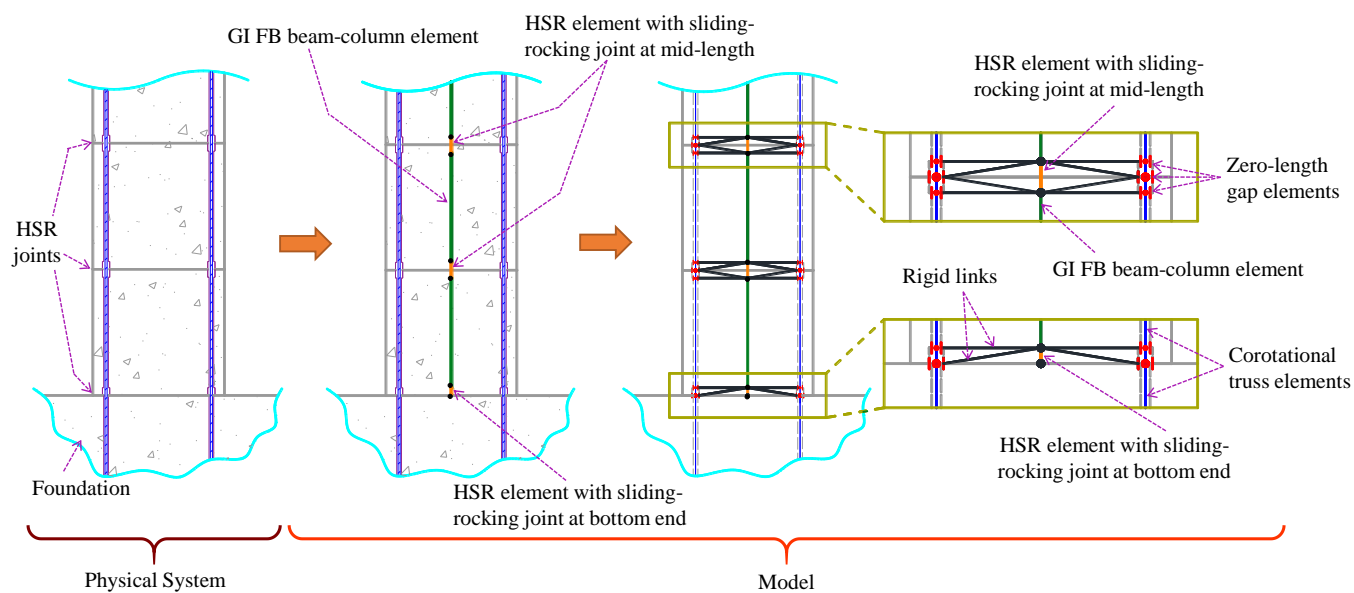
Fig. 6. Element configuration to simulate HSR columns

789
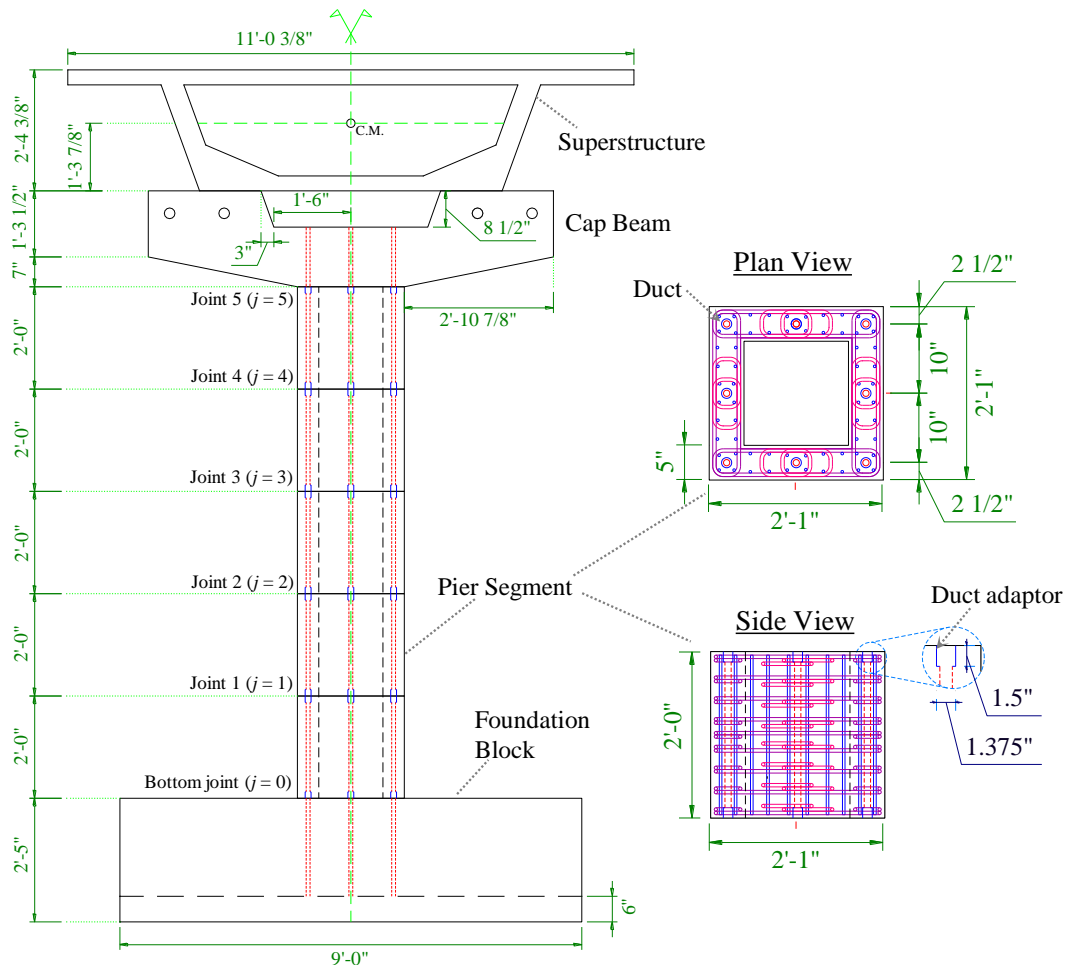
Fig. 7. HSR column test specimen
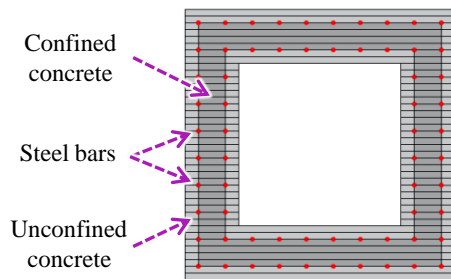
Fig. 8. Discretization of fiber sections
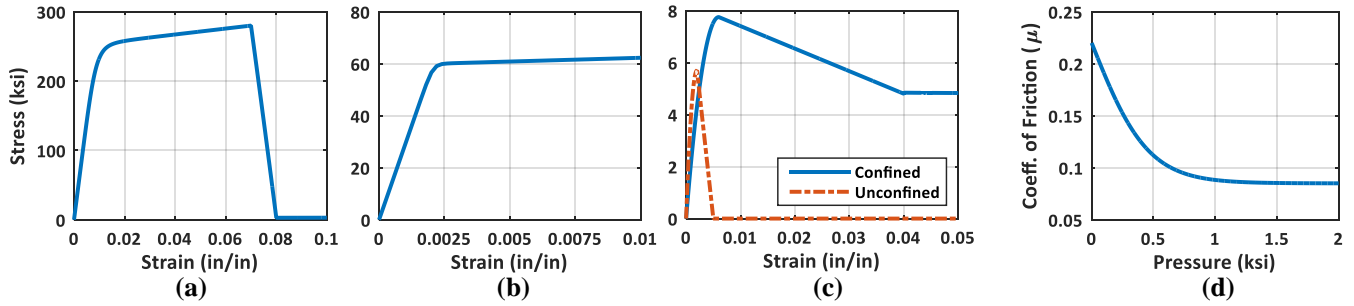
Fig. 9. Constitutive models: (a) tendon stress-strain backbone curve; (b) mild reinforcing steel stress-strain backbone curve; (c) concrete stress-strain backbone curves; and (d) coefficient of friction vs. pressure relationship
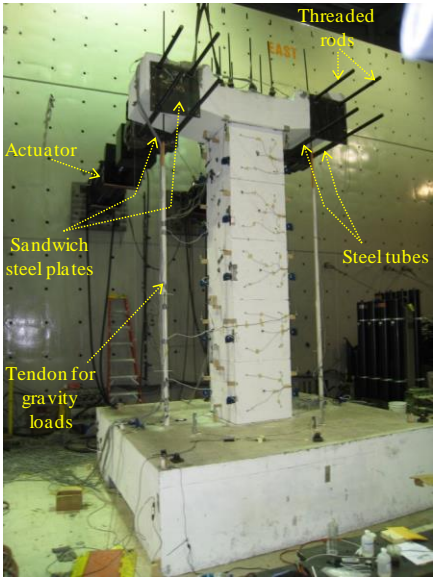
Fig. 10. Quasi-static test setup
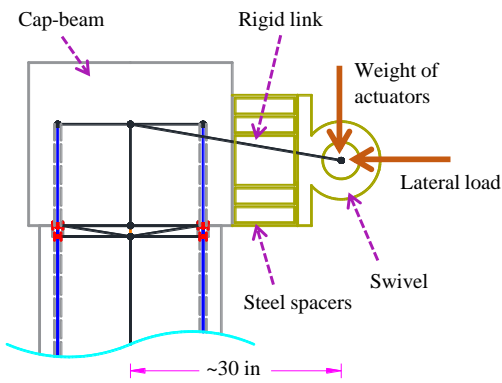
Fig. 11. Quasi-static test simulation: Location of applied loads and connection setup
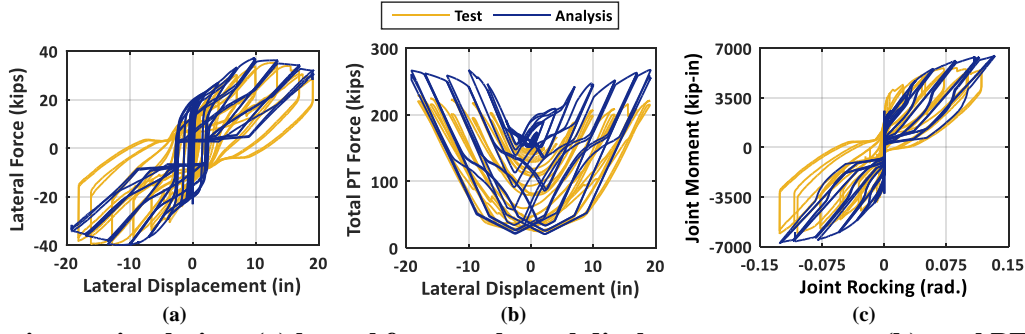
806
807 **Fig.** 12**. Quasi-static test simulation: (a) lateral force vs. lateral displacement response; (b) total PT force vs. lateral**
808   **displacement response; and (c) moment vs. rocking response at the bottom joint [1 kip = 4.45 kN, 1 in = 2.54 cm]**

809
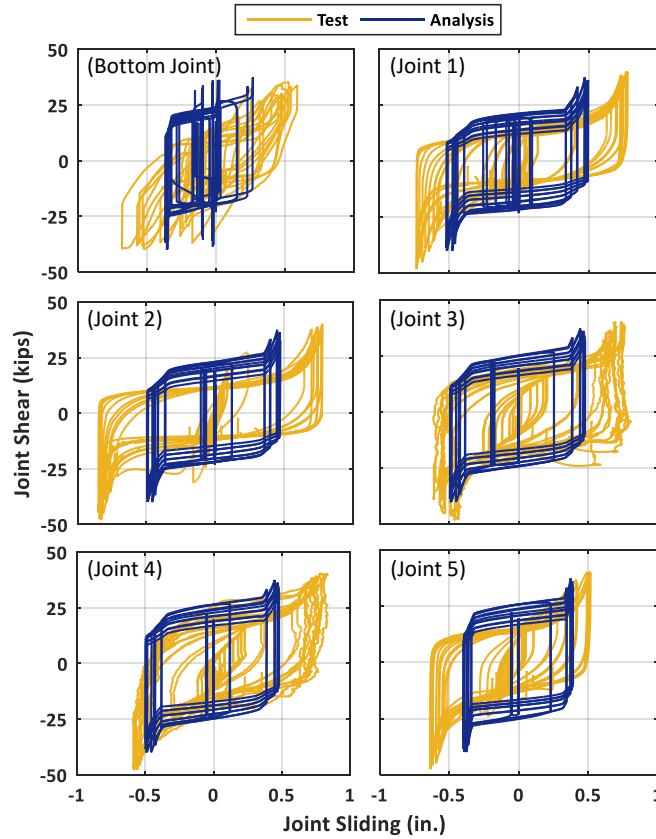
810
811 **Fig. 13. Quasi-static test simulation: Joint shear vs. sliding response. Joints are labeled per Fig. 7 [1 kip = 4.45 kN,**
812   **1 in = 2.54 cm].**

5

813
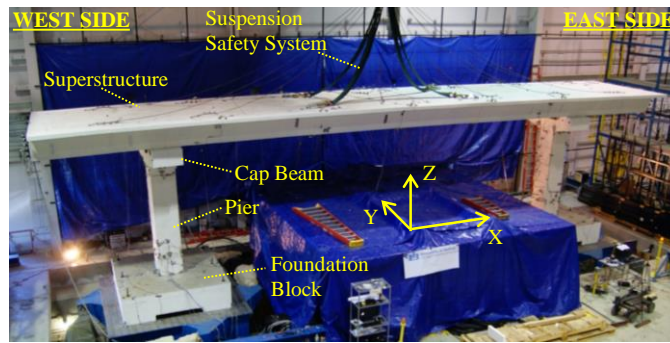
Fig. 14. Shake table test setup

816
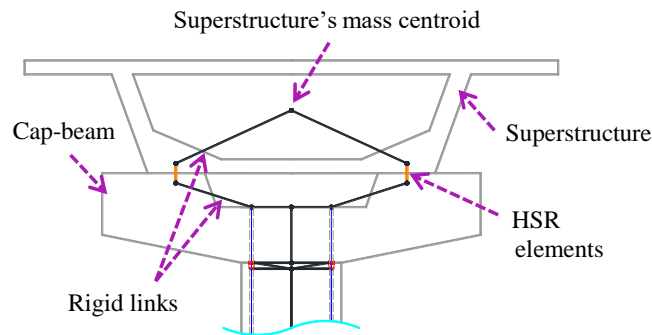
817
818   **Fig. 15. Shake table test simulation: Element configuration for superstructure-to-cap beam connectivity**
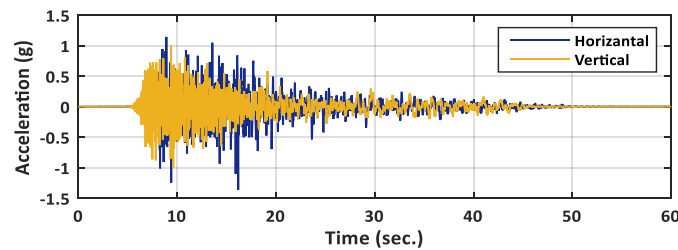
819

820
821   **Fig. 16. Shake table test simulation: Base acceleration time histories recorded during testing**
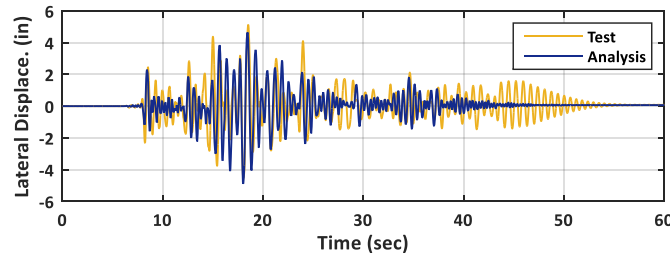
822

823
824   **Fig. 17. Shake table test simulation: Lateral displacement time histories at superstructure [1 in = 2.54 cm]**
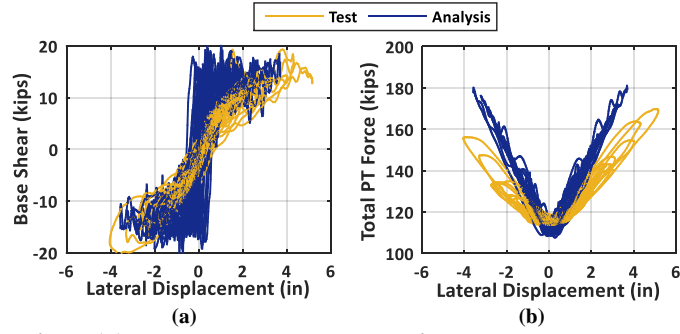
825

6

Fig. 18. Shake table test simulation: (a) base shear vs. lateral displacement at cap beam; and (b) total PT force vs. lateral displacement at cap beam [1 kips = 4.45 kN, 1 in = 2.54 cm]
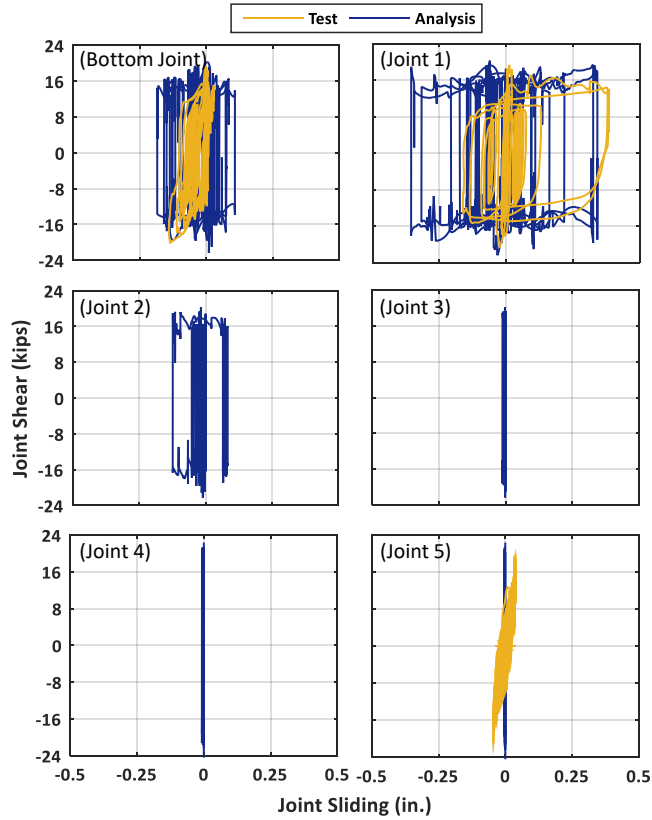

Fig. 19. Shake table test simulation: Joint shear vs. sliding responses [1 kips = 4.45 kN, 1 in = 2.54 cm]